Journal of Materials Science: Materials in Electronics (2019) 30:19792–19803
https://doi.org/10.1007/s10854-019-02345-2

Thermal oxidation of sputtered nickel nano-film as hole transport layer for high performance perovskite solar cells

Mustafa Aboulsaad[1,2] · Ayman El Tahan[3] · Moataz Soliman[2] · Said El-Sheikh[4] · Shaker Ebrahim[2]

Received: 17 July 2019 / Accepted: 3 October 2019 / Published online: 19 October 2019

Abstract
The effect of rapid oxidation temperature on the sputtered nickel (Ni) films to act as a hole transport layer (HTL) for perovskite solar cell (PSCs) was investigated. A nano-sputtered Ni film with a thickness about 100 nm was oxidized at a range of different oxidation temperatures between 350 and 650 °C to work as HTL in an inverted p–i–n configuration. DC Hall measurement in van der Pauw configuration and photoluminescence spectroscopy were used to measure the charge's mobility and extraction of nickel oxide (NiO) films. The behaviour of the carrier concentration measurements of NiO layers at different oxidation temperatures showed that the Ni layer oxidized at 450 °C had the highest carrier concentration among the other samples. The performance measurements of the fabricated PSCs showed that the nickel oxide hole-transporting layer which has been oxidized at the optimum oxidation temperature of 450 °C has the highest power conversion efficiency (PCE) of 12.05%. Moreover, the characteristic parameters of the optimum cell such as the open-circuit voltage (V_{OC}), short-circuit current density (J_{SC}) and fill factor (FF) were 0.92 V, 19.80 mA/cm^2 and 0.331, respectively.

1 Introduction

Perovskite materials can change their properties over the main three classifications of materials; conductor, insulator and semiconductor. They are denoted by ABX_3 structure as three different materials that can be combined with certain structure [1]. Metal halide perovskites as dyes under illumination can generate and transport of charge carriers in the perovskite solar cells (PSCs) [1]. Methylammonium lead triiodide ($CH_3NH_3PbI_3$) perovskite material started to be booming in the field of energy harvesting due to its excellent optoelectrical properties where it has a direct bandgap, wide range of solar spectrum absorption [2], high an absorption coefficient of 1.5×10^4 cm^{-1} at 550 nm [3], high charge carrier mobility of 66 cm^{-2} V s, small exciton binding energy with less than 10 meV [4], and long electron–hole diffusion length with up to 1 µm [5].

Due to the instability of the liquid electrolyte in solar cells, there are attempts to replace the liquid electrolyte with a solid material or quasi-solid material as was done in the dye-sensitized solar cells [6]. In perovskite solar cells, a hole transporting layer (HTL) is used instead of liquid electrolyte to extract hole carriers and transport them into the electrode [7, 8]. The commonly HTL is 2,2′,7,7′-tetrakis-(N,N-di-4-methoxyphenylamino)-9,9′-spirobifluorene (spiro-OMeTAD) which was reported over 2 decades [9, 10]. On the other hand, there are different materials from

Electronic supplementary material The online version of this article (https://doi.org/10.1007/s10854-019-02345-2) contains supplementary material, which is available to authorized users.

✉ Mustafa Aboulsaad
mustafa@uef.fi; mostafa.aboulsaad@alexu.edu.eg

Ayman El Tahan
amoussa73@yahoo.com

Moataz Soliman
msoliman@alexu.edu.eg

Said El-Sheikh
saidelsheikh@cmrdi.sci.eg

Shaker Ebrahim
shaker.ebrahim@alexu.edu.eg

[1] Institute of Photonics, Department of Physics and Mathematics, University of Eastern Finland, Joensuu Campus, 80100 Joensuu, Finland

[2] Department of Materials Science, Institute of Graduate Studies and Research, University of Alexandria, 163 Horreya Avenue, El-Shatby, Alexandria 21526, Egypt

[3] Department of Physics, Faculty of Science, University of Tanta, Qism 2, Gharbia Governorate, Tanta 31527, Egypt

[4] Department of Nanomaterials and Nanotechnology, Central Metallurgical Research and Development Institute, Cairo 11421, Egypt

inorganic, organic as well as hybrid materials to employ for extracting holes from perovskite.

In the current work, nickel oxide (NiO) is applied as HTL in an inverted configuration of $CH_3NH_3PbI_3$ based PSCs. NiO is a p-type material with wide bandgap energies, which has been used as HTL in organic and inorganic optoelectronic devices [11]. Chen et al. constructed an inverted planar configuration of perovskite solar cell that achieved power conversion efficiency (PCE) over 16% when they used a composite of Li Mg Ni O [12]. There are different processes to prepare and deposit NiO such as solution-processed [13], evaporation [14], spray pyrolysis or sputtering [15]. Furthermore, there are several working temperatures of NiO or Ni for annealing or oxidation processes ranging between 275 and 550 °C [11]. Hence, choosing the deposition method, working temperature, or the preparation technique is depending on the application of the work. Although the solution-processed of NiO is a cost-effective technique, there is a lack of the uniformity of the film at high temperature. Lai et al. [16] studied the effect of different oxidation temperatures of NiO deposited onto indium tin oxide (ITO) sheets on the performance of PSCs and they reported that the maximum efficiency at 450 °C was 7.75%. However, ITO substrate is instable at high oxidation temperatures [17], and the resistivity of the sheets is increased with increasing the temperature [18] which may affect the result of the cell performance.

The aim of this work is to homogenize a physical sputter of Ni layers which act as HTL in PSCs by oxidizing them at different temperatures. Furthermore, the effect of the oxidation temperatures ranging between 350 and 650 °C of Ni films formed onto the top of fluorine tin oxide (FTO) sheets and their influence on the performance of the perovskite solar cells were studied and evaluated.

2 Experimental work

2.1 Materials

Hydroiodic acid (57 wt% in ethanol), methylamine (CH3NH2) (40 wt% in aqueous solution), dimethyl sulfoxide (DMSO) (extra pure > 99%), and dimethylformamide (DMF) (extra pure > 99%) were purchased from Across company. Lead iodide (99.998%) and toluene were purchased from Alfa Aesar. Phenyl-C61-butyric acid methyl ester (PCBM) (99%) and diethyl ether (99%) were purchased from Ossila and Fisher scientific. Lithium fluoride (99%) was obtained from Sigma Aldrich. Ni target was fabricated in a local company with purity (99.8%). Finally, fluorine tin oxide (FTO) with a sheet resistance of 15 Ω/□ used as a photoelectrode for the perovskite solar cell. All stated materials have been used as received without further purification.

2.2 Preparation of methylammonium iodide

Methylammonium iodide (CH_3NH_3I) was synthesized using the procedure reported by Wang et al. [19]. 30 mL of HI was reacted dropwise with 27.86 mL of CH_3NH_2 in a 250 mL round bottom flask for 2 h with maintaining the reaction temperature at 0 °C with continuous stirring. Using rotary evaporator, the mixture was maintained at 50 °C to evaporate the solvent and white-yellowish precipitation of CH_3NH_3I was formed. Then, the precipitated powder was collected, washed with ethanol and diethyl ether three times for further purification by stirring the solution for 30 min for each wash, then dried under vacuum at 60 °C overnight. The dried powder was stored inside a glove box for further usage.

2.3 Preparation of methylammonium lead triiodide

Methylammonium lead triiodide ($CH_3NH_3PbI_3$) was synthesized according to the reported procedures of Maria Konstantakou et al. with some modification in the ratios [20]. CH_3NH_3I was mixed with PbI_2 with 1:1 molar ratio in mixed solvents of DMSO: DMF with 0.7:0.3 mL/mL. The final solution was stirred overnight at room temperature.

2.4 Device fabrication

FTO-coated glass substrates were cleaned by ultrasonication using distilled water, acetone, ethanol and isopropanol for 15 min for each solvent. These substrates were dried under nitrogen gas to remove any solvent residuals [21]. A 100 nm thick Ni was sputtered using DC sputtering (Hummer 8.1) at 70 W for 5 min onto the surface of cleaned FTO. Then, the sputtered layers were oxidized rapidly at 350, 450, 550 and 650 °C in a muffle furnace. The process was carried out by adjusting the controller of the furnace to reach the desired temperature for each sample in 60 min. Once the desired temperature was reached, the annealing time was maintained for 90 min to allow oxidation. Before deposition of perovskite material, NiO layers were heated at 40 °C to enhance the activity of the surface to get a well-deposited layer of perovskite. In glove box, $CH_3NH_3PbI_3$ was deposited on NiO surface through one-step spin-coating deposition technique for 40 s divided as follow; the first 10 s the layer was deposited at 1000 rpm to allow a uniform distribution of the solution on the surface, after that, the spinner was raised at 4000 rpm for the remaining 30 s. For enhancing the surface and crystal structure of perovskite layer, a 700 µL toluene was vigorously added after 30 s from the whole time to allow the quenching of the grain size of the active layer to occur [20, 22]. The role of the toluene is to add nonsolvent that does not dissolve perovskite material but is miscible

with DMSO and DMF to remove the residual solvents that do not evaporate [20, 22]. The final layers were annealed on a hotplate at 120 °C for 25 min. Then, a filtered prepared solution of PCBM (20 mg PCBM/1 mL chlorobenzene) was deposited by spin coating at 3000 rpm for 30 s [23], after that, the layers were annealed for 10 min at 60 °C.

Finally, using thermal evaporator, a very thin layer from LiF was deposited on the surface of the PCBM layer, then, a silver thin film was deposited as a counter electrode. The role of using LiF with PCBM is to avoid the hot metal particles from penetrating the PCBM layer causing direct contact between the active layer and the counter electrode [24]. Figure 1 shows the configuration of the fabricated PSCs layers in this study and its energy diagram. The valence band (VB) of NiO is properly positioned for extracting photoexcited holes from the valence band of $CH_3NH_3PbI_3$ active layer. It is worth noting the effect of the hole selective contact as well as the position of its valence band on the performance of the cell. The existence of HTL influences on the series resistance (R_S) of the device where the R_S decreases in the devices with HTL while it contributes to the whole resistance significantly in the cells without HTL [25]. In addition, the devices with HTL exhibits high V_{OC} and low recombination losses, which enhance the collected power from the device [25]. Effect of the position of the hole transporting layer valence band on the performance of carrier's extraction is relevant due to the other factors that affect the carrier extraction process such as the applied voltage and the selective contact resistance (R_{SC}) itself [25, 26]. However, in terms of absolute values, the closeness of the position of VB of the HTL to the position of the VB of the active layer promotes the hole relaxation between their valence bands [26].

2.5 Characterization techniques of NiO thin films

2.5.1 Ultraviolet–visible (UV–Vis) spectroscopy

The transmission and absorption spectra of NiO thin films were obtained in the range of 400–900 nm using UV–Vis spectrophotometer (Evolution 600 double beam scanning spectrophotometer, Thermo Scientific, USA).

2.5.2 Photoluminescence (PL)

Photoluminescence is the re-emission of light after absorption of incident photons by semiconductor materials with energy greater than bandgap energy (Eg). The excited carriers in higher energy levels relax to the available level in ground state by emitting a photon. Photoluminescence measurements were recorded for the active layer at an excitation wavelength of 440 nm. PL measurements were carried out at room temperature with a fluorescence spectrophotometer (Perkin Elmer LS-55).

2.5.3 X-ray diffraction (XRD)

X-ray diffraction scans were obtained using X-ray 7000 Shimadzu (Japan) at room temperature. The Bragge angle has (2θ) the range from 10 to 80 degree to study the crystallinity of the prepared films. The X-ray source is a Cu target generated at 30 kV and 30 mA with a scan speed of 4 deg/min.

2.5.4 Scanning electron microscopy (SEM)

The surface of different films was investigated using scanning electron microscopy (SEM "JEOL JSM-6360 LA", Japan) to study morphology and the homogeneity of the surface. Thin films of gold were sputtered onto the samples to get charge-free surfaces.

2.5.5 Hall measurements

HMS-5000 Hall Effect Measurement System Ecopia (Korea) is used to measure the conductivity, carrier mobility and carrier concentration of prepared NiO thin films.

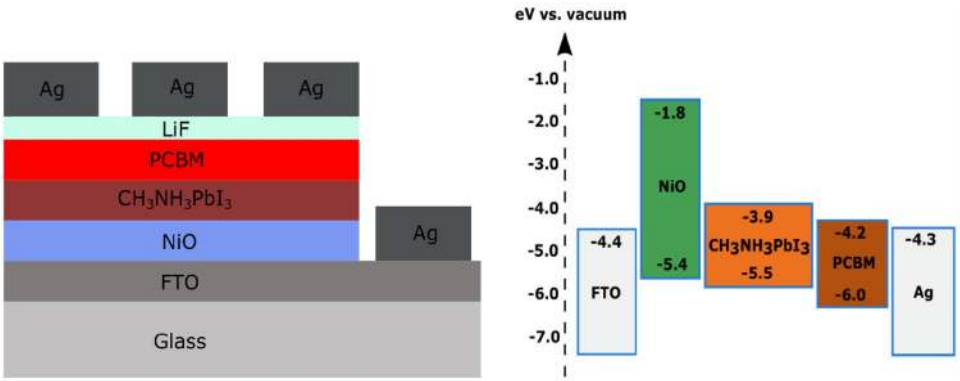

Fig. 1 Schematic diagram of the fabricated PSCs based on the inverted planar configuration of FTO/NiO/$CH_3NH_3PbI_3$/PCBM/LiF/Ag and the energy diagram of p–i–n perovskite solar cell using nickel oxide as hole extraction layer [27–29]

2.6 Performance measurement of perovskite photovoltaic cell

The current–voltage characteristics were performed for the fabricated photovoltaic cells under both dark and illumination conditions using computerized KEITHLEY series 2635A system source meter instruments controlled by TSP Express Software. The measurements have been performed using a Xenon lamp, which has been calibrated using standard PV cell.

3 Results and discussion

3.1 Optical properties of NiO

Due to the inverted planar configuration of the device, highly transmittance of HTM is needed to allow highly absorption spectrum for the perovskite layer. Hence, the transparency percentage (T%) of the NiO layer has been measured as a function of oxidation temperature. As shown in Fig. 2, the transmittance degree of 450 and 350 °C is about 80% between wavelength ranges 500–600 nm, while for 550 and 650 °C the transmittance is decreased by ~ 10% for the same interval of wavelength. The average transmittance spectra values over the whole wavelength range for 350, 450, 550 and 650 °C are 80.25, 75.62, 71.56 and 68.26%, respectively. To understand the behaviour of transmittance of the film, it is required to interrupt the relationship between the wavelength-dependent refractive index n(λ) with the transmittance of the film. The relation has been proposed by

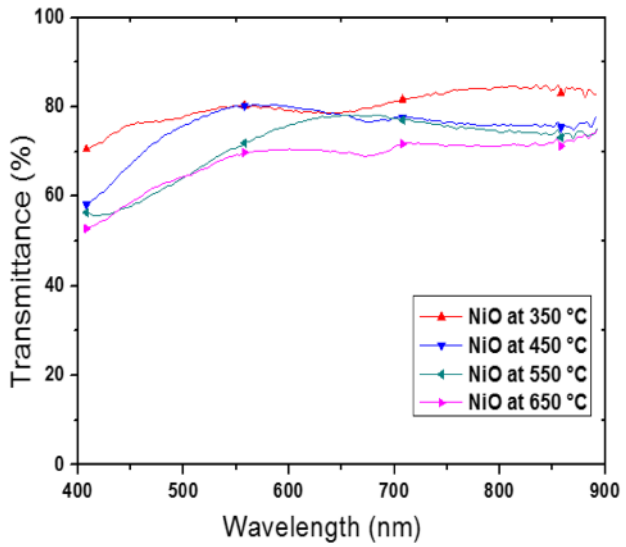

Fig. 2 Transmittance spectra of NiO layers oxidized at different temperatures

Sreemany et al. to calculate n(λ) with respect to T % [30]. Equation 1 estimates the value of n(λ):

$$n(\lambda) = \sqrt{n_o n_2}\left[\frac{1+\sqrt{1-T(\lambda)}}{T(\lambda)}\right], \quad (1)$$

where n_o and n_2 are the refractive index of air and FTO substrate, respectively. From the equation, there is an inverse proportional relation between the wavelength-dependent refractive index of the film and the transmittance value.

In addition, the measurements of the oxidation temperature-dependent bandgap energy have been studied. There is a fluctuation of the bandgap energy as the oxidation temperature increases, where the measurements confirmed the bandgap energy behaviour as reported by Venter et al. [31]. The oxidized nickel film at 450 °C recorded the highest bandgap energy of 3.65 eV while the bandgap energies of nickel films oxidized at 350, 550 and 650 °C are 3.46, 3.48 and 3.59 eV, respectively. Figure 3 shows the optical absorbance spectra of oxidized nickel films at different temperatures as well as the bandgap energy of NiO layers using Tauc method [32].

The charge transfer process between the perovskite and HTL is also dominated by the perovskite/HTL interface, which can be evaluated by the steady-state photoluminescence (PL) measurement as displayed in Fig. 4. The measurement has been done under excitation wavelength at 440 nm for the stack of glass/perovskite and glass/NiO/perovskite. As shown in Fig. 4, there is a radiative recombination peak at 738 nm for the perovskite layer. Apparently, NiO shows a significant PL quenching, indicating holes extraction and transfer at NiO/perovskite interface effectively. To understand the behaviour of NiO film that has been oxidized at 450 °C and its apparent effective extraction of holes from perovskite film, we need to consider the study which has been carried by S. Hietzschold et al. about the effect of annealing temperature on the work function of NiO films [33]. They have shown that the work function of NiO films at 400 °C was less than the work function at 325 °C, which promote the carrier extraction of NiO film. As a result, according to the calculated bandgap energies in this work, the maximum bandgap energy was for the oxidized nickel film at 450 °C, which has the lowest work function, and this allows extract carriers greater than the one with high work function.

3.2 Crystallinity of NiO layers

The heat treatment process on metals, which is characterized by a large number of very small metal crystals interlocked together cause changes in the mechanical properties and crystal structures of these metals [34]. At a certain temperature, the metal starts to oxidize where there is

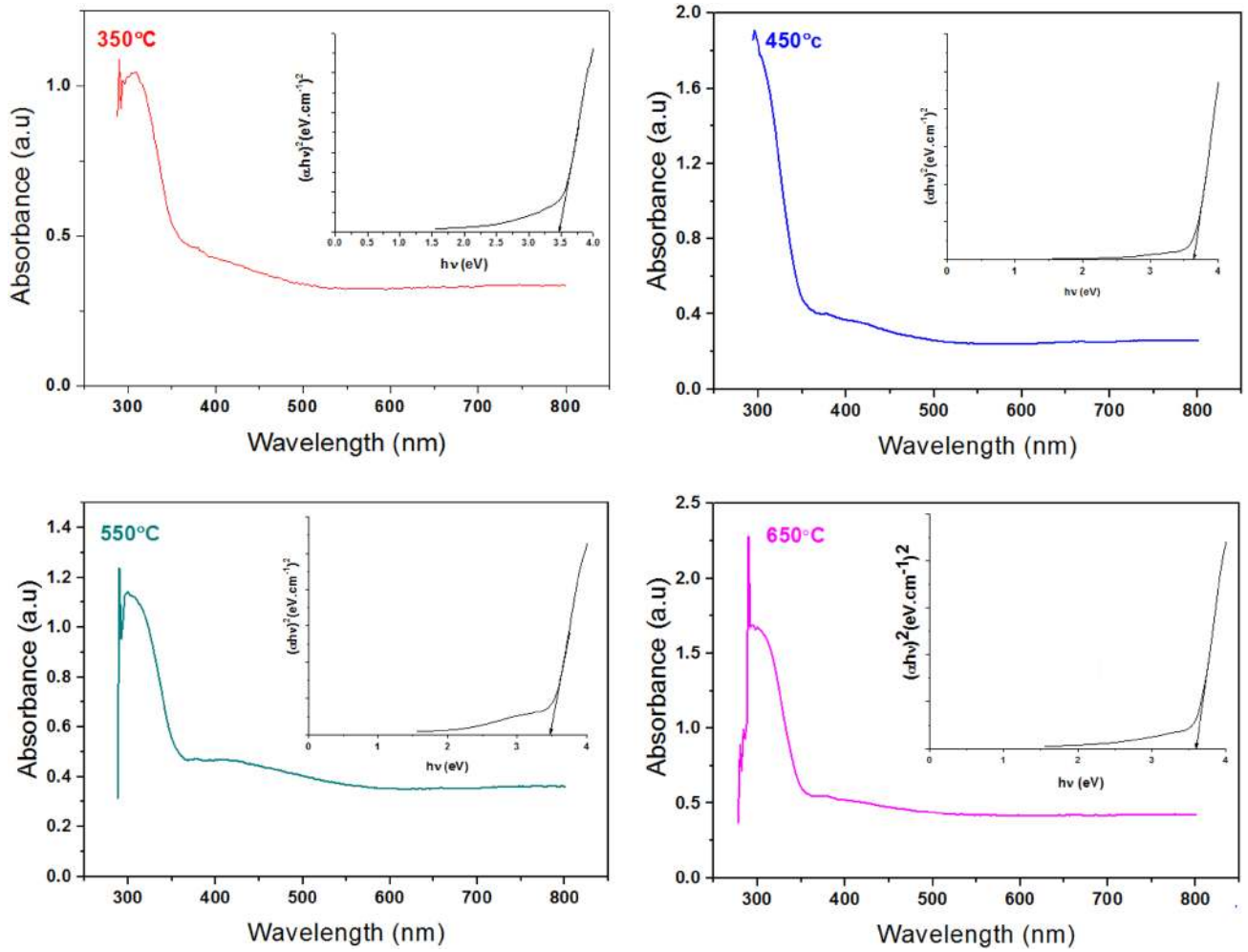

Fig. 3 Optical absorption spectra for nickel films oxidized at 350, 450, 550 and 650 °C. The insets show the $(\alpha h\nu)^2$ versus hν curve for the samples

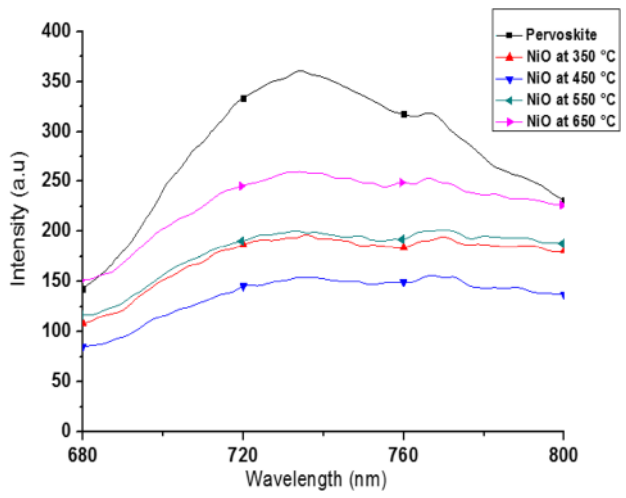

Fig. 4 PL spectra of glass/perovskite and glass/NiO/perovskite oxidized at different temperatures under an excitation wavelength of 440 nm

chemical diffusion of oxygen ions in the crystal structure of the metal that controls the nonstoichiometric properties of the metal oxide as well as the crystal parameters of its lattice [34]. Furthermore, in the case of nickel, there are different oxidation temperatures that depend on the preparation method, the precursor of the material and the oxidation kinetics [11, 13, 15, 35]. However, the most common oxidation temperature of the nickel-metal precursor is 350 °C [35]. Figure 5 shows the X-ray diffraction patterns of NiO on the top of the FTO substrate at different oxidation temperatures. The pattern shows a high peak at $2\theta = 38°$ which corresponds to the crystalline (111) plane of NiO monoclinic crystal structure as well as the formation of a weak peak at $2\theta = 62.5°$ which corresponds to the (220) plane of NiO. In addition, due to the rapid oxidation of nickel layer, there is a random small peak of crystalline NiO_2 and Ni_2O_3 monoclinic crystal structure at $2\theta = 66.372°$ of (004) plane, and a weak peak of cubic crystal structure nickel

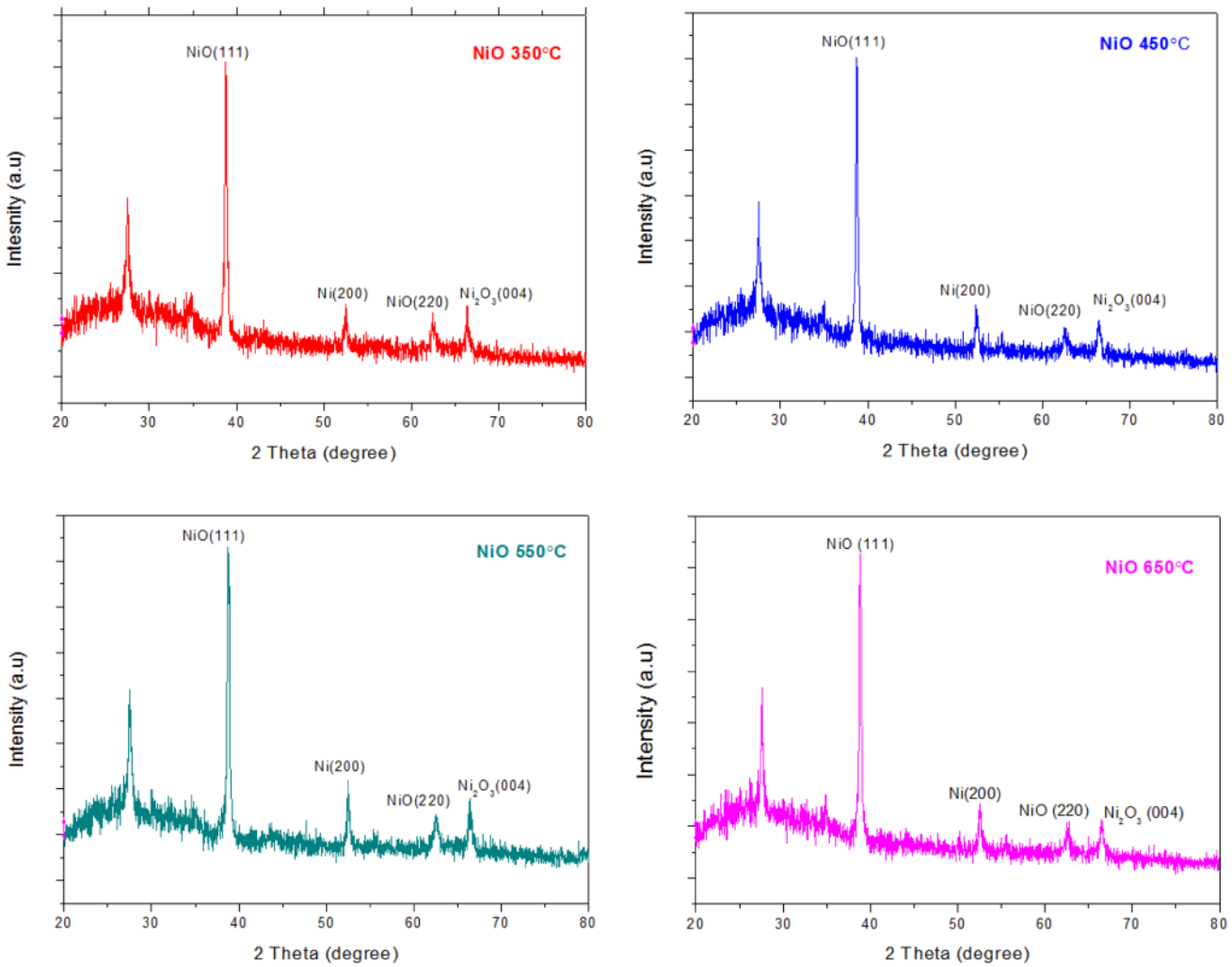

Fig. 5 XRD patterns for NiO films prepared on glass/FTO substrate

metal of plane (200) at 2θ = 52.5°. On the other hand, at 350 °C, there was an overlapping of (-111) plane of NiO_2 at 2θ = 38°, while there was an overlapping of (020) of NiO_2 at 2θ = 66.372° for all oxidation temperatures. The calculated d-spacing of NiO (111), NiO (220), Ni_2O_3 (004), and Ni (200) were approximately 2.35, 1.5, 1.4, and 1.7 A°, respectively [36, 37]. The heat treatment of Ni films to form NiO layers revealed the incomplete incorporation of oxygen with Ni, which was shown by the Ni atom signal in XRD analysis for all oxidation temperatures. This clearly shows the effect of the rapid oxidation on the composition of the film as well as the morphology of the films as seen in SEM images. The amount of crystalline phase of Ni_2O_3 indicates that Ni^{3+} ions formed as Ni_2O_3 phase rather than the incorporation with NiO matrix [38]. The crystallinity of the nickel films oxidized at different oxidation temperatures was investigated. Table 1 estimates the crystallinity index of the prepared NiO thin films.

Table 1 The crystallinity degree of the prepared NiO films at different oxidation temperatures

Oxidation temperature [°C]	Crystallinity percentage [%]
350	23.80
450	24.70
550	27.90
650	25.60

3.3 Morphological property of NiO layers

Surface morphology of NiO layers onto the glass substrate was investigated using scanning electron microscopy as presented in Fig. 6. The surface morphology of NiO film at 350 °C shows no cracks due to the suitable limit

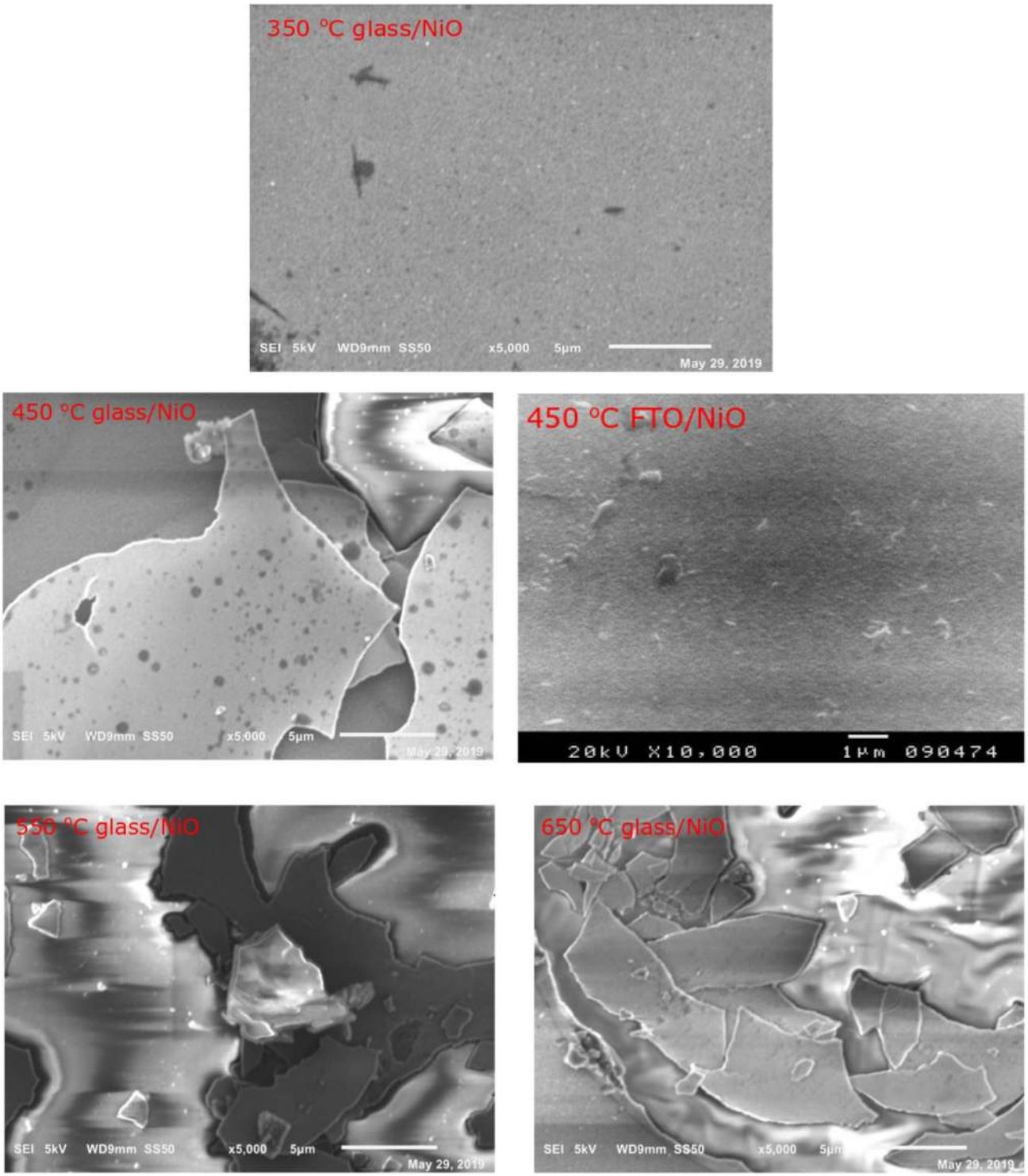

Fig. 6 SEM images of the NiO films at different oxidation temperatures

of temperature. For NiO film at 450 °C, due to the rapid increase of the oxidation temperature, the film suffers from large cracks and pinholes along the surface of the film. Moreover, as the oxidation temperature increases in the case of 550 and 650 °C, the cracks in the film's surface increase due to the high temperature. On the other hand, the surface of NiO layer that has been oxidized at the optimum oxidation temperature (450 °C) has been investigated on the top of FTO to compare with the one on the glass substrate. As shown in the Fig., the film is well aligned on the

surface of FTO due to the activity of the surface to accept the NiO layer. In the case of the glass substrate, the activity of the surface is low in comparison with the FTO surface that influences on the interface between NiO/FTO bilayer. Moreover, we observed small black spots on the NiO sheets at 350 °C, which could be related to Ni metal. However, by increasing the reaction temperature to 450–650 °C, the Ni metals begin to grow into NiO, forming gradually separated grains (defective or non-uniformly structure) of NiO layers with some uncompleted Ni–O reaction on the sample. These unreacted Ni metal on NiO layers would increase the sample conductivity during the experiments with the formation of more electrons.

3.4 Hall measurements

The carrier mobility, conductivity and carrier concentrations of NiO thin films were measured and studied by Hall effect. Table 2 describes the relations between the oxidation temperatures and the carrier mobility, carrier concentration and conductivity. The Hall effect displays as p-type NiO thin films resulting from the positive sign of Hall coefficient. The values of the Hall parameters show the effect of the rapid oxidation on the formation of pinholes in the surface of the films with relative low carrier mobility and conductivity. The behaviours of the carrier mobility and conductivity are almost the same due to the rule of charge carriers to conduct the charge inside the film, while the behaviour of the carrier concentration is different due to the scrambling of the carriers which obstacle the flow of the carriers inside the film. The measured crystallinity indexes of the films at different oxidation temperatures showed a small fluctuation in the crystallinity degree at which the oxidized Ni film at 350 °C has amorphous phases higher than the oxidized film at 450 °C. In addition, both films have amorphous phases higher than the oxidized films at 550 and 650 °C. Consequently, these amorphous phases boost the conductivity and carrier mobility in the case of 350 and 450 °C greater than 550 and 650 °C. Moreover, the defects and contaminated amount of Ni at low oxidation temperature increases the conductivity of the film due to their metal properties than the oxide film. The unexpected behaviour of the conductivity at the oxidation temperature of 650 °C is due to the rapid oxidation temperature that causes rapid diffusion paths of the defects during oxidation time [39]. The process in Fig. 7 shows the general oxidation process of the Ni layer, while the equivalent equation clarifies the presence of the Ni vacancies, electron–holes as the predominant defects in nickel oxide, as well as Ni^{2+} which can transform into Ni^{3+} (2 Ni ions must be transformed for each vacancy) equivalent to the formation of Ni_2O_3 in NiO matrix. There is a long-standing controversy about the type of conduction in NiO films and the role of the defects in this process [40]. Moreover, there are extensive studies that have been performed on the bulk samples [41]; however, there are only limited studies on the oxidation kinetics of thin metal films [41]. As mentioned early, NiO is a p-type semiconductor with the predominant defects of cation vacancies and electron-holes [35] whose resistivity can be lowered by an increase of the hole concentration: this can be achieved by an increase of Ni^{3+} ions resulting from the presence of the native defects, such as nickel vacancies and/or interstitial oxygen [42]. The XRD data shows the presence of Ni^{+3} ions in all samples, so the possible explanation

Table 2 The carrier mobility, carrier concentrations and conductivity of NiO thin films vs. the oxidation temperatures

Oxidation temperature [°C]	Carrier mobility [cm^2/Vs]	Carrier concentration [cm^{-3}]	Conductivity [$\Omega^{-1}\ cm^{-1}$]
350	3.49×10^{3}	7.58×10^{11}	4.24×10^{-4}
450	2.8×10^{-1}	1.5×10^{15}	6.86×10^{-5}
550	5.57×10^{-3}	4.96×10^{14}	4.43×10^{-7}
650	4.16×10^{2}	8.80×10^{11}	5.87×10^{-5}

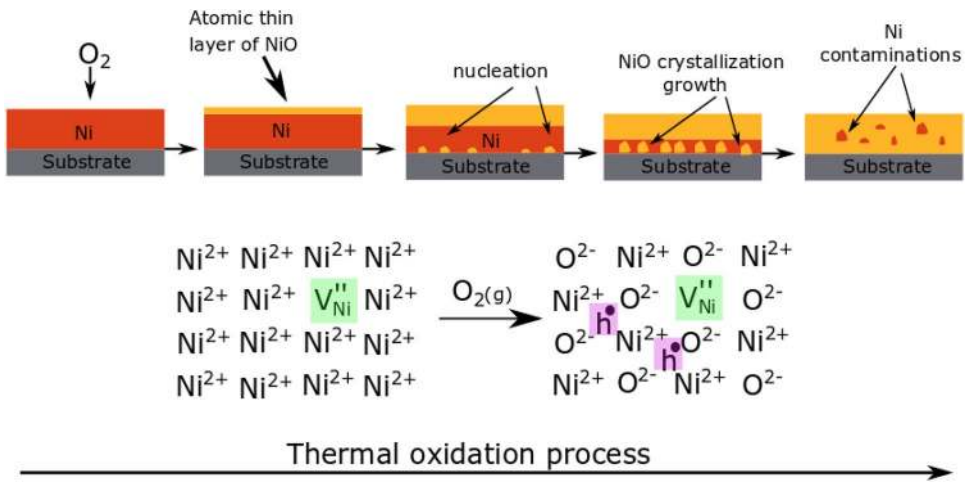

Fig. 7 The general thermal oxidation process of the Ni layer and the equivalent equation for the formation of Ni vacancies and electron-holes during the oxidation process of NiO

is the fluctuation of these ions over the oxidation process of different oxidation temperatures. Furthermore, Hwang et al. [43] considered the point defects of NiO as a function of temperature which confirm our explanation in this work. In that study, the coordination number of Ni–Ni increased with increasing annealing temperature, which may be a result of the nickel vacancies greatly decreasing with increasing temperature. The temperature-dependent resistivity of NiO films has two paths; the changing in temperature during the oxidation process which is contributed to increasing the resistivity with increasing the oxidation temperature and increasing the annealing temperature of NiO films after deposition which enhance the conductivity due to the semiconductor nature of NiO films [42, 44, 45]. Furthermore, as reported in previous works [42, 44, 45], the electrical resistivity of NiO films is located between the ranges of 10–10^6 (Ω cm) which is the range of the electrical resistivity reported in this work. However, the very high resistivity of the NiO films in this work is an apparent indication of the difference between the effect of the rapid oxidation process and the handled process of NiO thin films.

3.5 J–V characteristics of the fabricated perovskite solar cells

Effect of oxidation temperature of sputtered NiO films as HTL on the photovoltaic performance of the fabricated FTO/NiO/$CH_3NH_3PbI_3$/PCBM/LiF/Ag perovskite solar cells is investigated. The resultant J–V curves of the PSCs with different oxidation temperature of NiO HTLs under the condition of AM 1.5 and Pin of 50 mW/cm^2 carried by Keithly power source are shown in Fig. 8. The measurements show that NiO film rapidly oxidized at 450 °C has the optimum photovoltaic parameters and the maximum efficiency. On optical excitation of the perovskite active layer, charge transfer from $CH_3NH_3PbI_3$ into PCBM occurs where PCBM acts as an electron acceptor layer. The difference in the electron injection rate is assigned to differences in energy band alignment at the interfaces. The charge carrier recombination back to the ground state can be happened to be at least one order of magnitude faster in the $CH_3NH_3PbI_3$/PCBM. As explained in PL measurements, the low performance of NiO layers, which have been oxidized at 550 and 650 °C is due to the cracks at the surface morphology at higher temperatures that affect the extraction of the carriers at the interface. The PSCs with NiO HTL oxidized at 450 °C exhibit a high performance with PCE of 12.05%, Jsc of 19.80 mA/cm^2, Voc of 0.92 V and FF of 33%. Table 3 estimates the performance parameters of NiO HTLs in PSCs with a maximum power conversion efficiency of 12.05% at 450 °C NiO film. Table 4 exhibits the best performance of NiO-based planar PSCs in recent years of the same main configuration (NiO/perovskite/PCBM) as in this work using sputtering as the deposition technique for NiO and oxidized Ni as HTLs.

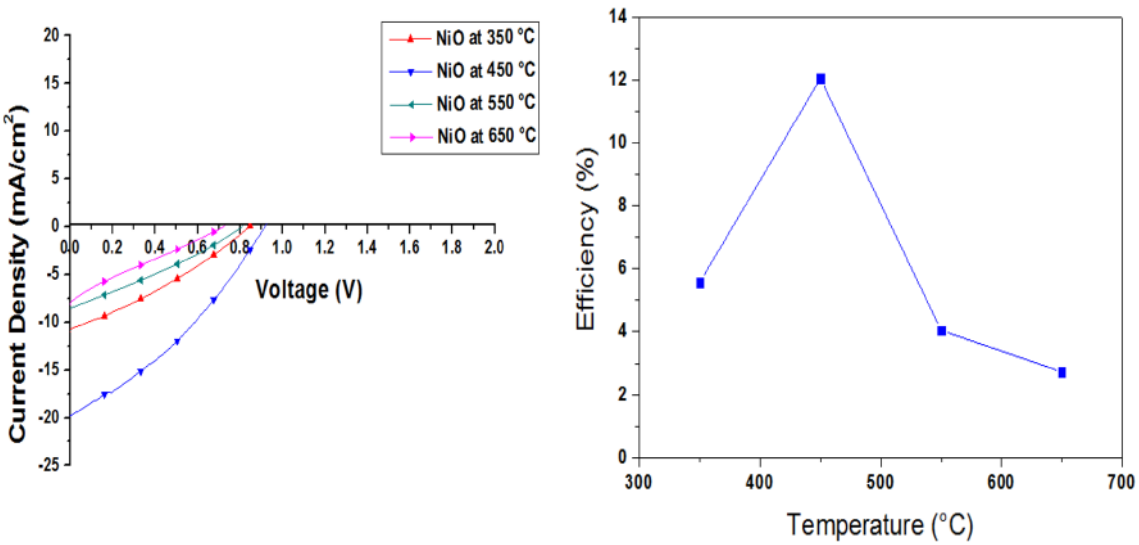

Fig. 8 J–V curves of PSCs with NiO HTL oxidized at different oxidation temperatures and the calculated efficiency vs. oxidation temperatures of sputtered Ni films

Table 3 Photovoltaic parameters of FTO/NiO/$CH_3NH_3PbI_3$/PCBM/LiF/Ag at different oxidation temperatures of NiO films

Temperature [°C]	V_{oc} [V]	J_{sc} [mA/cm^2]	FF	PCE [%]	Area [cm^2]	P_{in} [mW/cm^2]
350	0.84	10.73	0.309	5.57	0.097	50
450	0.92	19.80	0.331	12.05	0.194	50
550	0.8	8.56	0.296	4.05	0.194	50
650	0.72	7.97	0.238	2.73	0.194	50

Table 4 Performances of the reported planar PSCs based on undoped c-NiO films as well as the performance of the NiO (oxidized at 450 °C) based planar PSC in this work

Device configuration	V_{oc} [V]	J_{sc} [mA/cm^2]	FF	PCE [%]	Area [cm^2]	Method	Ref.
FTO/NiO/MAPbI$_3$[a]/PCBM/LiF/Ag	0.92	19.80	0.331	12.05	0.194	Oxidation of sputtered Ni	CW[b]
FTO/NiO/$MAPbI_3$/PCBM/Ag	1.10	15.17	0.59	9.84	NA	Directly sputtered NiO	[46]
ITO/NiO/$MAPbI_3$/PCBM/BCP[c]/Ag	0.98	19.69	0.64	12.4	0.1	Directly sputtered NiO	[47]
FTO/NiO/$MAPbI_3$/PCBM/Au	1.03	23.77	0.54	13.26	0.07	Directly sputtered NiO	[48]
FTO/NiO_x/$MAPbI_3$/PCBM/BCP/Ag	1.06	20.68	0.74	16.20	0.09	Directly sputtered NiO	[49]

[a]Methylamine lead iodide

[b]Current work

[c]Bathocuproine

4 Conclusion

In conclusion, the effect of oxidation temperatures of NiO films as hole-transporting layers for perovskite solar cells was evaluated. From Hall measurements, there was a sharp decrease in the efficiency for temperature degrees of 550 and 650 °C, which indicate that the optimum working oxidation temperature of NiO film is 450 °C. Due to the rapid oxidation, there were low values of the conductivity, carrier mobility and carrier concentrations of the other temperature degrees. The PSCs with NiO oxidized at 450 °C exhibited a high performance with PCE of 12.05%, Jsc of 19.80 mA/cm^2, Voc of 0.92 V and FF of 33%.

Acknowledgements Open access funding provided by University of Eastern Finland (UEF) including Kuopio University Hospital. We thank our colleagues from the Department of Advanced Materials, Institute of Central Metallurgical Research and Development, especially Professor Said El-Sheikh for assistance with Hall measurements. In addition, we would like to show our gratitude to Mohamed Samir, research assistant, IGSR, Donia Said, M.Sc, the University of Eastern Finland, and Enas Mustafa, M.Sc, Rovira I Virgili University for sharing assistance with us throughout the work.

References

1. L. Calió, S. Kazim, M. Grätzel, S. Ahmad, Hole-transport materials for perovskite solar cells. Angew. Chem. Int. Ed. **55**, 14522–14545 (2016)
2. S. Kazim, M.K. Nazeeruddin, M. Grätzel, S. Ahmad, Perovskite as light harvester: a game changer in photovoltaics. Angew. Chem. Int. Ed. **53**, 2812–2824 (2014)
3. A. Kojima, K. Teshima, Y. Shirai, T. Miyasaka, Organometal halide perovskites as visible-light sensitizers for photovoltaic cells. J. Am. Chem. Soc. **131**, 6050–6051 (2009)
4. T.J. Savenije, C.S. Ponseca, L. Kunneman, M. Abdellah, K. Zheng, Y. Tian, Q. Zhu, S.E. Canton, I.G. Scheblykin, T. Pullerits, Thermally activated exciton dissociation and recombination control the carrier dynamics in organometal halide perovskite. J. Phys. Chem. Lett. **5**, 2189–2194 (2014)
5. Q. Dong, Y. Fang, Y. Shao, P. Mulligan, J. Qiu, L. Cao, J. Huang, Solar cells. Electron-hole diffusion lengths > 175 μm in solution-grown $CH_3NH_3PbI_3$ single crystals. Science **347**, 967–970 (2015)
6. G. Magdy, M.E. Harb, A.M. Elshaer, L. Saad, S. Ebrahim, M. Soliman, Preparation of electrolytic quasi-solid-state nanofibers for dye-sensitized solar cells. JOM **71**, 1944–1951 (2019)
7. M.M. Lee, J. Teuscher, T. Miyasaka, T.N. Murakami, H.J. Snaith, Efficient hybrid solar cells based on meso-superstructured organometal halide perovskites. Science **338**, 643–647 (2012)
8. H.S. Kim, C.R. Lee, J.H. Im, K.B. Lee, T. Moehl, A. Marchioro, S.J. Moon, R. Humphry-Baker, J.H. Yum, J.E. Moser, Lead iodide perovskite sensitized all-solid-state submicron thin film mesoscopic solar cell with efficiency exceeding 9%. Sci. Rep. **2**, 591 (2012)
9. U. Bach, D. Lupo, P. Comte, J.E. Moser, F. Weissçrtel, J. Salbeck, H. Spreitzer, M. Grätzel, Solid-state dye-sensitized mesoporous TiO_2 solar cells with high photon-to-electron conversion efficiencies. Nature **395**, 583–585 (1998)

10. J. Krgger, R. Plass, L. Cevey, M. Piccirelli, M. Grätzel, U. Bach, High efficiency solid-state photovoltaic device due to inhibition of interface charge recombination. Appl. Phys. Lett. **79**, 2085–2087 (2001)
11. M.H. Li, P.S. Shen, K.C. Wang, T.F. Guo, P. Chen, Inorganic p-type contact materials for perovskite-based solar cells. J. Mater. Chem. A **3**, 9011–9019 (2015)
12. W. Chen, Y. Wu, Y. Yue, W. Zhang, X. Yang, H. Chen, E. Bi, I. Ashraful, M. Grätzel, L. Han, Efficient and stable large-area perovskite solar cells with inorganic charge extraction layers. Science **350**, 944–948 (2015)
13. J.R. Manders, S.W. Tsang, M.J. Hartel, T.H. Lai, S. Chen, C.M. Amb, J.R. Reynolds, F. So, Solution-processed nickel oxide hole transport layers in high efficiency polymer photovoltaic cells. Adv. Funct. Mat. **23**, 2993–3001 (2013)
14. T. Abzieher, S. Moghadamzadeh, F. Schackmar, H. Eggers, F. Sutterlüti, A. Farooq, D. Kojda, K. Habicht, R. Schmager, A. Mertens, R. Azmi, L. Klohr, J.A. Schwenzer, M. Hetterich, U. Lemmer, B.S. Richards, M. Powalla, U.W. Paetzold, Electron-beam-evaporated nickel oxide hole transport layers for perovskite-based photovoltaics. Adv. Energy Mater. **9**, 1802995 (2019)
15. J. Cui, F. Meng, H. Zhang, K. Cao, H. Yuan, Y. Cheng, F. Huang, M. Wang, $CH_3NH_3PbI_3$-based planar solar cells with magnetron-sputtered nickel oxide. ACS Appl. Mater. Interfaces **6**, 22862–22870 (2014)
16. W.C. Lai, K.W. Lin, T.F. Guo, J. Lee, Perovskite-based solar cells with nickel-oxidized nickel oxide hole transfer layer. IEEE Trans. Electron Devices **62**, 1590–1595 (2015)
17. C.H. Yang, S.C. Lee, S.C. Chen, T.C. Lin, The effect of annealing treatment on microstructure and properties of indium tin oxides films. Mater. Sci. Eng. B **129**, 154–160 (2006)
18. F. Li, C. Chen, F. Tan, C. Li, G. Yue, L. Shen, W. Zhang, Semi-transparent inverted polymer solar cells employing a sol-gel-derived TiO_2 electron-selective layer on FTO and MoO_3/Ag/MoO_3 transparent electrode. Nanoscale Res. Lett. **9**, 579 (2014)
19. J.H. Im, C.R. Lee, J.W. Lee, S.W. Park, N.G. Park, 6.5% efficient perovskite quantum-dot-sensitized solar cell. Nanoscale **3**, 4088–4093 (2011)
20. M. Konstantakou, D. Perganti, P. Falaras, T. Stergiopoulos, Anti-solvent crystallization strategies for highly efficient perovskite solar cells. Crystals **7**, 291 (2017)
21. V. More, V. Shivade, P. Bhargava, Effect of cleaning process of substrate on the efficiency of the DSSC. Trans. Indian Ceram. Soc. **75**, 59–62 (2016)
22. N.J. Jeon, J.H. Noh, Y.C. Kim, W.S. Yang, S. Ryu, S. Il Seok, Solvent engineering for high-performance inorganic-organic hybrid perovskite solar cells. Nat. Mater. **13**, 897–903 (2014)
23. K. Lee, J. Ryu, H. Yu, J. Yun, J. Lee, J. Jang, Enhanced efficiency and air-stability of NiO_X-based perovskite solar cells via PCBM electron transport layer modification with triton X-100. Nanoscale **9**, 16249–16255 (2017)
24. N.M. Schmerl, J.S. Quinton, G.G. Andersson, On the growth of evaporated LiF on P3HT and PCBM. J. Phys. Chem. C **122**, 23420–23431 (2018)
25. E.J.J. Pérez, M. Wussler, F.F. Santiago, K.L. Wollny, E. Mankel, T. Mayer, W. Jaegermann, I.M. Sero, Role of the selective contacts in the performance of lead halide perovskite solar cells. J. Phys. Chem. Lett. **5**, 680–685 (2014)
26. Z. Song, S.C. Watthage, A.B. Phillips, M.J. Heben, Pathways toward high-performance perovskite solar cells: review of recent advances in organo-metal halide perovskites for photovoltaic applications. J. Photonics Energy **6**, 022001 (2016)
27. S.S. Malia, C.K. Hong, p-i-n/n-i-p type planar hybrid structure of highly efficient perovskite solar cells towards improved air stability: synthetic strategies and the role of p-type hole transport layer (HTL) and n-type electron transport layer (ETL) metal oxides. Nanoscale **8**, 10528–10540 (2016)
28. E. Li, Y. Guo, T. Liu, W. Hu, N. Wang, H. He, H. Lin, Preheating-assisted deposition of solution-processed perovskite layer for an efficiency-improved inverted planar composite heterojunction solar cell. RSC Adv. **6**, 30978–30985 (2016)
29. J. Zhang, F. Li, K. Yang, C.P. Veeramalai, T. Guo, Low temperature processed planar heterojunction perovskite solar cells employing silver nanowires as top electrode. Appl. Surf. Sci. **369**, 308–313 (2016)
30. M. Sreemany, S. Sen, A simple spectrophotometric method for determination of the optical constants and band gap energy of multiple layer TiO_2 thin films. Mater. Chem. Phys. **83**, 169–177 (2004)
31. A. Venter, J.R. Botha, Optical and electrical properties of NiO for possible dielectric applications. S. Afr. J. Sci. **107**, 1–2 (2011)
32. J. Tauc, Optical properties and electronic structure of amorphous Ge and Si. Mater. Res. Bull. **3**, 37–46 (1968)
33. S. Hietzschold, S. Hillebrandt, F. Ullrich, J. Bombsch, V. Rohnacher, S. Ma, W. Liu, A. Köhn, W. Jaegermann, A. Pucci, W. Kowalsky, E. Mankel, S. Beck, R. Lovrincic, Functionalized nickel oxide hole contact layers: work function versus conductivity. ACS Appl. Mater. Interfaces **9**, 39821–39829 (2017)
34. A. Jayendran, *Englisch für maschinenbauer*, 2nd edn. (Springer, Germany, 1997), pp. 43–49
35. S. Mrowec, Z. Grzesik, Oxidation of nickel and transport properties of nickel oxide. J. Phys. Chem. Solids **65**, 1651–1657 (2004)
36. L.D.L.S. Valladares, A. Ionescu, S. Holmes, C.H.W. Barnes, A.B. Domínguez, O.A. Quispe, J.C. González, S. Milana, M. Barbone, A.C. Ferrari, H. Ramos, Y. Majima, Characterization of Ni thin films following thermal oxidation in air. J. Vac. Sci. Technol. **32**, 051808 (2014)
37. U. Kwon, B.G. Kim, D.C. Nguyen, J.H. Park, N.Y. Ha, S.J. Kim, S.H. Ko, S. Lee, D. Lee, H.J. Park, Solution-processible crystalline NiO nanoparticles for high-performance planar perovskite photovoltaic cells. Sci. Rep. **6**, 30759 (2016)
38. N. Srivastava, P.C. Srivastava, Realizing NiO nanocrystals from a simple chemical method. Bull. Mater. **33**, 653–656 (2010)
39. R. Haugsrud, On the high-temperature oxidation of nickel. Corros. Sci. **45**, 211–235 (2003)
40. P. Lunkenheimer, A. Loidl, C.R. Ottermann, K. Bange, Correlated barrier hopping in NiO films. Phys. Rev. B **44**, 5927 (1991)
41. Y. Unutulmazsoy, R. Merkle, D. Fischer, J. Mannhart, J. Maier, The oxidation kinetics of thin nickel films between 250 and 500 °C. Phys. Chem. Chem. Phys. **19**, 9045–9052 (2017)
42. H. Sato, T. Minami, S. Takato, T. Yamada, Transparent conducting p-type NiO thin films prepared by magnetron sputtering. Thin Solid Films **236**, 27–31 (1993)
43. W.L. Jang, Y.M. Lu, W.S. Hwang, T.L. Hsiung, H.P. Wang, Point defects in sputtered NiO films. Appl. Phys. Lett. **94**, 062103 (2009)
44. A.J. Varkey, A.F. Fort, Solution growth technique for deposition of nickel oxide thin films. Thin Solid Films **235**, 47–50 (1993)
45. D. Adler, L.H. Tjeng, F.C. Voogt, T. Hibma, G.A. Sawatzky, C.T. Chen, J. Vogel, M. Sacchi, S. Iacobucci, Temperature and thickness dependence of magnetic moments in NiO epitaxial films. Phys. Rev. B **57**, 11623 (1998)
46. J. Cui, F.P. Meng, H. Zhang, K. Cao, H.L. Yuan, Y.B. Cheng, F. Huang, M.K. Wang, CH3NH3PbI3-based planar solar cells with magnetron-sputtered nickel oxide. ACS Appl. Mater. Interfaces **6**, 22862–22870 (2014)

47. H. Lee, Y.T. Huang, M.W. Horn, S.P. Feng, Engineered optical and electrical performance of rf–sputtered undoped nickel oxide thin films for inverted perovskite solar cells. Sci. Rep. **8**, 5590 (2018)
48. P. Yang, J. Wang, X. Zhao, J. Wang, Z. Hu, Q. Huang, L. Yang, Magnetron-sputtered nickel oxide films as hole transport layer for planar heterojunction perovskite solar cells. Appl. Phys. A **125**, 481 (2019)
49. X. Yan, J. Zheng, L. Zheng, G. Lin, H. Lin, G. Chen, B. Du, F. Zhang, Optimization of sputtering NiO_x films for perovskite solar cell applications. Mater. Res. Bull. **103**, 150–157 (2018)